PNAS RESEARCH ARTICLE | BIOPHYSICS AND COMPUTATIONAL BIOLOGY

The full activation mechanism of the adenosine A_1 receptor revealed by GaMD and Su-GaMD simulations

Yang Li[a,b,1], Jixue Sun[a,1], Dongmei Li[a,2], and Jianping Lin[a,c,d,2]

Edited by Yinglong Miao, The University of Kansas, Lawrence, KS; received March 2, 2022; accepted September 14, 2022 by Editorial Board Member J. A. McCammon

The full activation process of G protein–coupled receptor (GPCR) plays an important role in cellular signal transduction. However, it remains challenging to simulate the whole process in which the GPCR is recognized and activated by a ligand and then couples to the G protein on a reasonable simulation timescale. Here, we developed a molecular dynamics (MD) approach named supervised (Su) Gaussian accelerated MD (GaMD) by incorporating a tabu-like supervision algorithm into a standard GaMD simulation. By using this Su-GaMD method, from the active and inactive structure of adenosine A_1 receptor (A_1R), we successfully revealed the full activation mechanism of A_1R, including adenosine (Ado)–A_1R recognition, preactivation of A_1R, and A_1R–G protein recognition, in hundreds of nanoseconds of simulations. The binding of Ado to the extracellular side of A_1R initiates conformational changes and the preactivation of A_1R. In turn, the binding of G_{i2} to the intracellular side of A_1R causes a decrease in the volume of the extracellular orthosteric site and stabilizes the binding of Ado to A_1R. Su-GaMD could be a useful tool to reconstruct or even predict ligand–protein and protein–protein recognition pathways on a short timescale. The intermediate states revealed in this study could provide more detailed complementary structural characterizations to facilitate the drug design of A_1R in the future.

G protein–coupled receptor | molecular dynamics simulations | ligand–protein recognition pathway | protein–protein recognition pathway | enhanced sampling method

G protein–coupled receptors (GPCRs) are the largest family of receptors in the cell membrane (1, 2). GPCRs recognize a variety of external molecules and initiate various intracellular signaling cascades as responses that ultimately regulate body growth, development, and metabolism. They are widely distributed in the human body and participate in a variety of physiological roles (3). More than 30% of the drugs on the market target GPCRs (4).

The adenosine A_1 receptor (A_1R) is one of the four subtypes of the G protein–coupled adenosine receptor family that mediate the biological effects of endogenous adenosine (Ado) (5). Activation of the A_1R is therapeutically desirable for ischemia-perfusion injury, atrial fibrillation, and neuropathic pain (6). Using regular A_1R orthosteric agonists has failed in the development of analgesics because of a lack of sufficient on-target selectivity as well as off-tissue adverse effects (7). However, an allosteric modulator of A_1R reported by Draper-Joyce et al. (8) exhibits analgesic efficacy. Moreover, an A_1R-selective agonist has been discovered by Wall et al. (9) to elicit analgesia without respiratory depression through selectively activating G_{ob} among the six $G_{i/o}$ subtypes. A_1R exists in a dynamic equilibrium between inactive and active states that can be selectively shifted by the binding of a ligand and through interaction with intracellular proteins such as $G_{i/o}$ (10). The biased agonists with selectivity for the particular A_1R conformational states are proposed as a better option for drug development by promoting $G_{i/o}$ signaling without affecting other pathways mediated by A_1R (11–14). Recently, the structural basis of A_1R with agonists/antagonists, allosteric modulators, and G proteins has attracted great interest, and great breakthroughs have been made. With the use of X-ray crystallography and cryo-electron microscopy (cryo-EM) technology, a considerable number of A_1Rs bound with agonists/antagonists, allosteric modulators, and G proteins have been resolved (8, 15–17). In 2017, Glukhova et al. (15) resolved the X-ray structure of A_1R bound to the selective covalent antagonist DU172 (Protein Data Bank [PDB] code 5UEN). In the same year, Cheng et al. (16) reported the structure of A_1R with a selective noncovalent antagonist PSB36 (PDB code 5N2S). These two structures, in which A_1R is in its inactive state, provide a molecular basis for A_1R subtype selectivity for antagonists. In 2018, Draper-Joyce et al. (17) revealed the cryo-EM structure of the A_1R–G_{i2} complex bound to its endogenous agonist Ado (Ado–A_1R–G_{i2} complex, PDB code 6D9H, 6D9H structure for short).

Significance

Clarifying the recognition pathways of agonist and G protein to G protein–coupled receptor (GPCR) is essential to understand the signal transduction mechanism of GPCR. However, it is still challenging to simulate the full activation process of GPCR on a reasonable simulation timescale with conventional molecular dynamics (MD) methods. Here, we developed an MD simulation approach named supervised Gaussian accelerated MD (Su-GaMD) and revealed the full activation mechanism of adenosine (Ado) A_1 receptor (A_1R) (including adenosine Ado−A_1R recognition, preactivation of A_1R, and A_1R−G protein recognition) in hundreds of nanoseconds simulations. The whole activation process and the metastable intermediate states revealed in this study could provide complementary structural characterizations to expand our perspectives on A_1R drug discovery.

The authors declare no competing interest.

This article is a PNAS Direct Submission. Y.M. is a guest editor invited by the Editorial Board.

[1]Y.L. and J.S. contributed equally to this work.

[2]To whom correspondence may be addressed. Email: dongmeili@nankai.edu.cn or jianpinglin@nankai.edu.cn.

This article contains supporting information online at http://www.pnas.org/lookup/suppl/doi:10.1073/pnas.2203702119/-/DCSupplemental.

Published October 10, 2022.

Most recently, they resolved the cryo-EM structure of the A_1R–G_{i2} complex bound to its endogenous agonist Ado and a positive allosteric modulator MIPS521 (MIPS521–Ado–A_1R–G_{i2} complex, PDB code 7LD3) (8). In these two structures, A_1R was fully activated with both Ado binding in the extracellular orthosteric pocket and G_{i2} protein binding in the intracellular region. The detailed characterizations of these structures provide a solid structural foundation for the activation of A_1R. However, the dynamic processes of ligand recognition, G_{i2} protein recognition, and full activation of A_1R have not been clarified. The experimentally observed ligand-bound states of A_1R are chemically stable and can be utilized for the design of A_1R-targeting drugs. In fact, the atomic-level description of the different metastable intermediate states characterized in the recognition process suggests complementary opportunities for the design of new A_1R drugs. Hopefully, the future of drug design will involve atomic details of not only the experimentally observed ligand-bound state but also the whole ligand–protein network of recognition pathways, including all metastable intermediate states (18). A complete understanding of the full activation process of A_1R (including the Ado recognition pathway, the G protein recognition pathway, and the full activation of A_1R) will help to expand our perspectives on A_1R drug discovery and development.

The dynamic process and recognition pathway of agonist–GPCR and GPCR–G protein are important to improve understanding of the signal transduction mechanism involved in the full activation process of GPCRs, while the full activation process occurs on a timescale of several milliseconds (19). The associated long timescale is difficult to access via conventional molecular dynamics (MD) simulations. Over the past decades, MD simulations have been applied to study the recognition and dissociation between ligands and GPCRs, including long-timescale conventional MD (cMD) (20, 21) and a variety of enhanced sampling MDs (21–28) including random acceleration MD (RAMD), steered MD (sMD), metadynamics (MTD), and accelerated MD (aMD). A detailed understanding of ligand-introduced GPCR activation has been developed in recent years, and GPCRs undergo significant conformational changes in extracellular and intracellular regions (2, 29, 30). Recently, Moro's group (31) provided the supervised MD (SuMD) approach, which combined a tabu-like supervision algorithm on the ligand–receptor approaching distance with cMD simulations, to study the binding event and pathway between an antagonist and $A_{2A}R$ at dozens of nanoseconds. Moreover, with the emergence of active X-ray or cryo-EM structures of GPCRs, many cMD and enhanced sampling MD simulations have been shown to be successful in studying the activation mechanism of GPCRs (25, 32–36). However, MD studies focusing on the interaction between GPCRs and intracellular proteins are scarce, even though many GPCRs combined with intracellular proteins have been resolved experimentally. Notably, McCammon's group (37) successfully simulated the binding of a G protein mimetic nanobody (Nb9-8) to the M_2 muscarinic acetylcholine receptor (M_2R) by using a Gaussian aMD (GaMD) method in a very long timescale simulation (4,500 ns). Due to the limitations of computational capacity, it is still very difficult to predict GPCR–G protein recognition pathways even with existing enhanced sampling MD methods.

Here, we provide a enhanced sampling technique (Su-GaMD) by incorporating a tabu-like supervision algorithm into a GaMD simulation. Su-GaMD can provide a more favorable way to discover the process by which GPCR interacts with ligand and intracellular protein at the nanosecond timescale. By using the Su-GaMD and GaMD methods, we simulated the Ado–A_1R binding event and then the recognition process of G_{i2} protein to A_1R based on both the active and inactive A_1R structures. The full activation mechanism of A_1R (including the Ado–A_1R recognition, the preactivation of A_1R, and the A_1R–G protein recognition) and the possible recognition pathways of Ado to A_1R and G_{i2} to A_1R were revealed. The conformational changes occurring in both the intracellular and extracellular binding pockets of A_1R were observed and the coupling between them was discussed. This study provides comprehensive insights into A_1R characterization during its whole activation process and opens up avenues for the rational design of A_1R drugs.

Results and Discussion

Design of the Su-GaMD Simulations. We developed the Su-GaMD method derived from SuMD and GaMD by exploiting a tabu-like supervision algorithm in a standard GaMD simulation. We used a simplified Ado–A_1R–$G\alpha_i$ model (with the α subunit of the G_{i2} protein [$G\alpha_i$] to present the heterotrimeric G_{i2} protein) to test the reliability of this Su-GaMD method. We placed $G\alpha_i$ >20 Å away from A_1R (system A, *SI Appendix*, Fig. S1*A*) and performed Su-GaMD simulations to reconstruct the A_1R–$G\alpha_i$ complex.

To select an appropriate time interval, we performed three independent Su-GaMD simulations for system A_1 (Fig. 1*C*) with time intervals of 300, 600, and 900 ps. Each simulation was replicated three times. In all the simulations, $G\alpha_i$ was successfully observed to enter the intracellular binding site of A_1R in less than 50 ns of the Su-GaMD simulation (Fig. 1*A* and Table 1 and *SI Appendix*, Table S1). During A_1R–$G\alpha_i$ recognition, the $G\alpha_i$ rmsd (defined as the rmsd calculated on the heavy atoms in the main chain of $G\alpha_i$ relative to the 6D9H structure) fell to ∼4.7 Å and the A_1R-$G\alpha_i$ distance (defined as the distance between the centers of mass [COMs] of the heavy atoms of the $G\alpha_i$ α5-helix [residues Lys331 to Phe355] and A_1R) dropped to ∼35.9 Å (which was close to that of 32.8 Å in the 6D9H structure) (Fig. 1*B* and *SI Appendix*, Table S1). These results indicated that the A_1R–$G\alpha_i$ complex close to the 6D9H structure was reconstructed through these Su-GaMD simulations. Considering a compromise of the sampling number and the simulation time, we chose the 600-ps interval (same as the previous SuMD works of Moro's group (38, 39)) for the following Su-GaMD simulations.

To test the influence of the initial position and orientation of $G\alpha_i$, we also performed Su-GaMD simulations for systems A_2, A_3, and A_4 (Fig. 1*C* and Table 1 and *SI Appendix*, Table S2). We found that $G\alpha_i$ could enter its binding site in A_1R and achieve an A_1R–$G\alpha_i$ complex similar to the 6D9H structure in a reasonable Su-GaMD simulation time no matter where we placed it or what its orientation was in the beginning.

For comparison, a 1,000-ns unsupervised GaMD simulation was performed for system A_1. We found that the stable A_1R–$G\alpha_i$ complex could not be reached in this extremely long-time GaMD simulation (the minimum $G\alpha_i$ rmsd was 25.8 Å, see *SI Appendix*, Fig. S4*B*). In addition, we performed three parallel Su-MD simulations (without Gaussian acceleration) for system A_1 and compared the results with those of Su-GaMD simulations. The $G\alpha_i$ rmsds and $G\alpha_i$–A_1R distances in the three replicates of Su-MD simulation are depicted in *SI Appendix*, Fig. S5. The mimimum $G\alpha_i$ rmsds and the minimum A_1R–$G\alpha_i$ distances of the Su-MD simulations are depicted in *SI Appendix*, Table S3. We found that the Su-MD simulations could reconstruct the A_1R–$G\alpha_i$ complex as well, but the simulation times were 45.0, 54.6, and 75.6 ns (*SI Appendix*, Fig. S5 and Table S3), which

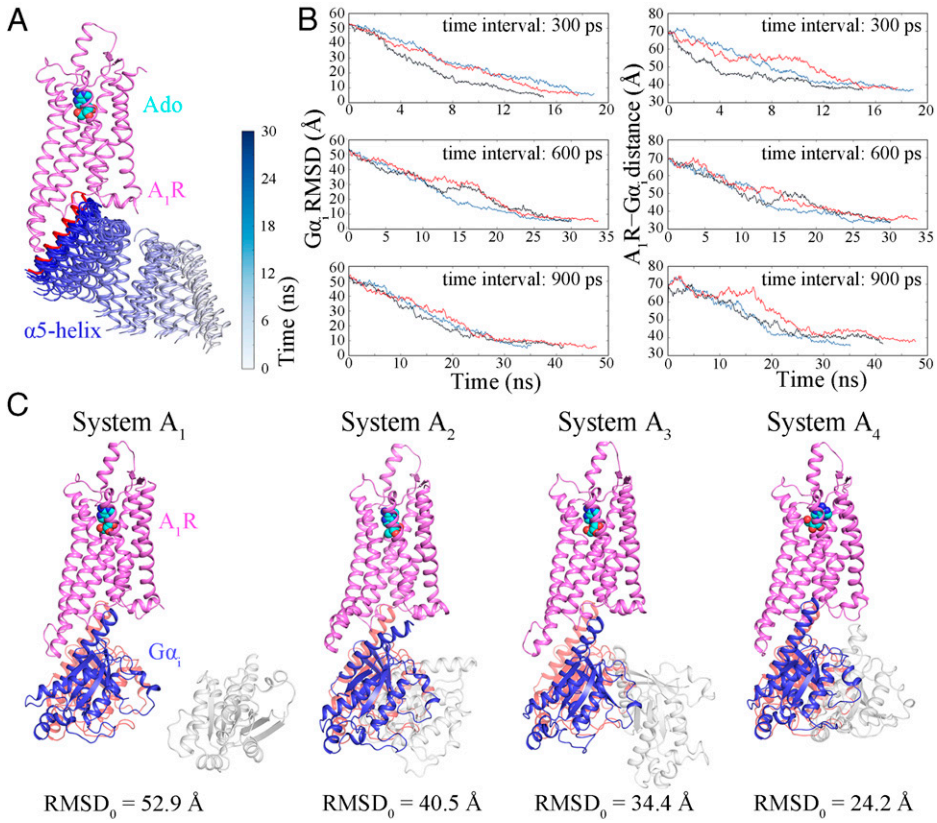

Fig. 1. (*A*) Recognition of $G\alpha_i$ (only the α5-helix is shown) to the intracellular binding site of A_1R. Trajectories of the α5-helix of $G\alpha_i$ (ribbons) are colored by simulation time on a silver (0 ns) to blue (30 ns) scale. The α5-helix of $G\alpha_i$ in the 6D9H structure is shown as a red ribbon. (*B*) Time-dependent $G\alpha_i$ rmsds and A_1R–$G\alpha_i$ distances using time intervals of 300, 600, and 900 ps. (*C*) Binding of $G\alpha_i$ to A_1R was observed in the trajectories of replicates with different initial positions and orientations of $G\alpha_i$. A_1R is colored violet, $G\alpha_i$ in the 6D9H structure is colored pink, the initial position of $G\alpha_i$ is shown in silver, and $G\alpha_i$ in the final snapshot is colored blue.

were longer than those of the Su-GaMD simulations (30.0, 30.0, and 33.6 ns; Fig. 1*B* and *SI Appendix*, Table S1). The mimimum $G\alpha_i$ rmsds of the Su-MD simulations were comparable to those of the Ga-SuMD simulations (4.6, 5.0, and 4.9 Å for Su-MD vs 4.9, 4.9, and 4.9 Å for Su-GaMD; *SI Appendix*, Tables S1 and S3), but the minimum A_1R–$G\alpha_i$ distances of the Su-MD simulations were longer than those of the Ga-SuMD simulations (37.0, 37.2, and 38.8 Å for Su-MD vs 33.6, 33.6, and 35.2 Å for Su-GaMD; *SI Appendix*, Tables S1 and S3). In summary, we could reconstruct the A_1R–$G\alpha_i$ complex in a binding mode similar to that of the 6D9H structure and observed the A_1R–$G\alpha_i$ recognition process in less than 50 ns by using the Su-GaMD strategy, while this $A_1R-G\alpha_i$ complex could not be reached even in long-time (e.g., 1,000 ns) unsupervised GaMD simulation. Further details are provided in *SI Appendix*. There was no overall conformational change of the receptor during the simulation of the A_1R–$G\alpha_i$ recognition process.

After the verification of this Su-GaMD method, we employed it to investigate the full activation mechanism of A_1R. The whole heterotrimeric G_{i2} protein, including $G\alpha_i$ and Gβγ, was employed for the rest of the simulations.

Reconstruction of the Ado–A_1R–G_{i2} Complex from the Active A_1R Structure. Ado–A1R recognition pathway.

To investigate the Ado–A_1R binding event, we performed Su-GaMD simulations for A_1R with Ado >20 Å away from its

Table 1. Overview of the simulations in the present study

System	Description	Method	Replicates	Time interval of Su-GaMD	Time* (ns)
A_1	A_1R–$G\alpha_i$ binding event ($rmsd_0$ = 52.9 Å)	Su-GaMD	3	300 ps	17.2
	A_1R–$G\alpha_i$ binding event	Su-GaMD	3	600 ps	31.2
	A_1R–$G\alpha_i$ binding event	Su-GaMD	3	900 ps	41.4
A_2	A_1R–$G\alpha_i$ binding event ($rmsd_0$ = 40.5 Å)	Su-GaMD	3	600 ps	25.0
A_3	A_1R–$G\alpha_i$ binding event ($rmsd_0$ = 34.4 Å)	Su-GaMD	3	600 ps	18.2
A_4	A_1R–$G\alpha_i$ binding event ($rmsd_0$ = 24.2 Å)	Su-GaMD	3	600 ps	30.0
B	Ado–A_1R binding event (from active A_1R)	Su-GaMD	3	600 ps	34.4
	A_1R–G_{i2} binding event	Su-GaMD	3	600 ps	40.2
C_1	Ado–A_1R binding event (from inactive A_1R)	Su-GaMD	3	600 ps	107.6
	Preactivation of A_1R	GaMD	3	–	150.0
C_2	A_1R–G_{i2} binding event	Su-GaMD	3	600 ps	61.6

*For each system, the Su-GaMD simulation time means the average value of three replicates.

orthosteric site (system B in Table 1, *SI Appendix*, Fig. S1*B*). Starting from free diffusion in the solvent, Ado gradually entered the extracellular binding site of A_1R composed of Thr91$^{3.36}$, Phe171^{ECL2}, Glu172^{ECL2}, Leu250$^{6.51}$, Asn254$^{6.55}$, Thr277$^{7.42}$, and His278$^{7.43}$ in a 25.8-ns Su-GaMD simulation (Fig. 2, Movie S1). The Ado rmsd (defined as the rmsd calculated on all the heavy atoms of Ado relative to the 6D9H structure) fell from 57.2 Å to 1.4 Å (Fig. 2*B*) and the Ado–A_1R distance (defined as the distance between the COMs of the heavy atoms of Ado and the residues Thr91$^{3.36}$, Phe171^{ECL2}, Glu172^{ECL2}, Leu250$^{6.51}$, Asn254$^{6.55}$, Thr277$^{7.42}$, and His278$^{7.43}$ that formed the Ado-binding pocket of A_1R) decreased from 58.2 Å to 0.7 Å (which was comparable to that of 1.1 Å in the 6D9H structure) during the Su-GaMD simulation (black line in *SI Appendix*, Fig. S6*B*). This indicated that the final binding pose of Ado in A_1R was close to that in the 6D9H structure at the end of the Su-GaMD simulation. During the simulation of the Ado–A_1R binding event, G_{i2} moved freely in the solvent and was >14.9 Å away from A_1R. Thus, the possible pathway of Ado–A_1R recognition was observed.

In the Ado–A_1R binding free energy landscape we calculated (from the active A_1R structure), the Ado–A_1R recognition process was found to involve several metastable intermediate states (Fig. 2*C*). Four metastable intermediate states (states 1, 2, 3, and 4) were identified (Fig. 2 *A* and *F*), in which the binding free energies between Ado and A_1R were −7.7, −13.1, −23.1, and −27.8 kcal·mol^{-1}, respectively (Fig. 2*C*, points 1, 2, 3, and 4). A detailed analysis of contact residues during the Ado–A_1R recognition process was also performed on the Su-GaMD trajectory, and all the residues of A_1R within 4 Å of Ado in the Su-GaMD simulation were shown in the contact map (Fig. 2*D*).

States 1, 2, 3, and 4 depict the Ado–A_1R recognition pathway along the Su-GaMD simulation time (Fig. 2 *A* and *F*). First (in state 1, at 4.875 ns), Ado interacted with A_1R through residues in TM1 (Ser6$^{1.29}$-Gln9$^{1.32}$), ECL3 (Ser267^{ECL3}), and TM7 (Tyr271$^{7.36}$) (state 1 in Fig. 2*D*). A hydrogen bond was observed between the 5′-hydroxyl oxygen in the ribose moiety of Ado and the hydroxyl hydrogen of Ser6$^{1.29}$ (state 1 in Fig. 2*F*). Then (in state 2, at 6.975 ns), Ado entered the extracellular vestibule consisting of residues in ECL2 (Glu170^{ECL2}-Lys173^{ECL2}), ECL3 (Lys265^{ECL3}), and TM7 (Pro266$^{7.31}$-Tyr271$^{7.36}$) (state 2 in Fig. 2*D*). The ribose moiety of Ado was accommodated by the side chains of Glu170^{ECL2}, Glu172^{ECL2}, and Lys265^{ECL3} through the hydrogen bonds between them, and the nitrogen in the 6-amino group of the purine ring in Ado formed a hydrogen bond with the hydrogen in the phenylhydroxyl group of Tyr271$^{7.36}$ (state 2 in Fig. 2*F*). After that (in state 3, at 18.750 ns), Ado entered the site that approximate to the 6D9H binding conformation and formed stable contacts with ECL2 (residues Phe171^{ECL2} and Glu172^{ECL2}) and TM5-TM7 (Met177$^{5.35}$ and Ser246$^{6.47}$-Thr270$^{7.35}$) (state 3 in Fig. 2*D*). The ribose moiety of Ado formed hydrogen bonds with residues Asn254$^{6.55}$, Thr257$^{6.58}$, and Lys265^{ECL3} (state 3 in Fig. 2*F*). Finally (in state 4, at 25.350 ns), Ado reached the orthosteric binding site of A_1R, making contact with TM3, ECL2, and TM5-TM7 (residues Val87$^{3.32}$, Leu88$^{3.33}$, Thr91$^{3.36}$, Phe171^{ECL2}, Glu172^{ECL2}, Met177$^{5.35}$, Met180$^{5.38}$, Leu250$^{6.51}$, His251$^{6.52}$, Asn254$^{6.55}$, Ile274$^{7.39}$, and Thr277$^{7.42}$) (state 4 in Fig. 2*D*). Asn254$^{6.55}$ located the purine ring of Ado through two hydrogen bonds, and notable interactions between Ado and the orthosteric site residues included π-π stacking with Phe171^{ECL2} and hydrogen bonds with Glu172^{ECL2} and Thr277$^{7.42}$ (state 4 in Fig. 2*F*). Accordingly, the Su-GaMD simulation revealed the Ado–A_1R binding event. We observed the possible recognition pathway and summarized all the amino acids involved in the binding event. ECL2 and ECL3 were important during recognition. The binding pathway of Ado and its metabolite inosine to $A_{2A}R$ has been explored successfully with the SuMD method by Moro's group (40, 41).

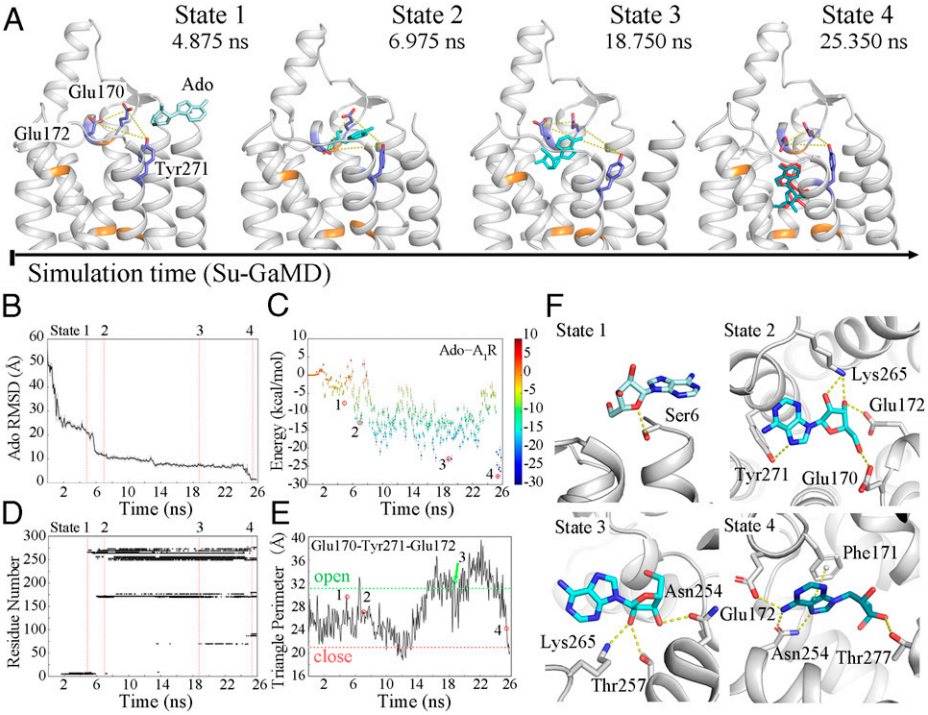

Fig. 2. (*A*) The Ado–A_1R recognition process. A_1R is shown in silver; residues Thr91$^{3.36}$, Phe171^{ECL2}, Leu250$^{6.51}$, Asn254$^{6.55}$, Thr277$^{7.42}$, and His278$^{7.43}$ are shown in orange; and Glu170^{ECL2}, Glu172^{ECL2}, and Tyr271$^{7.36}$ are shown as blue sticks. Ado is shown as a cyan stick, and the pose of Ado in the 6D9H structure is colored red in state 4. Time-dependent (*B*) Ado rmsd, (*C*) binding free energy landscape for Ado–A_1R, (*D*) Ado–A_1R contact residues, and (*E*) the triangle perimeters of the Glu170^{ECL2}–Tyr271$^{7.36}$–Glu172^{ECL2} vestibular lid during the recognition process (the triangle perimeters of the open and closed states are depicted in green and red dashed lines). (*F*) The four metastable intermediate states in the Ado–A_1R recognition pathway.

Most recently, the A_1R recognition and dissociation of five endogenous, selective and nonselective agonists, namely, the binding and unbinding pathways to A_1R, were simulated by Deganutti et al. (36) using SuMD. In our present study, most of the key residues involved in states 1, 2, 3, and 4 (i.e., $Glu170^{ECL2}$, $Phe171^{ECL2}$, $Glu172^{ECL2}$, $Asn254^{6.55}$, $Thr257^{6.58}$, $Lys265^{ECL3}$, $Tyr271^{7.36}$, and $Thr277^{7.42}$) were identified to compose the orthosteric or allosteric site in previous mutational and computational studies of ligand interactions in A_1R (15, 36, 42–44).

Three independent Su-GaMD simulations were performed and produced similar results. The Ado rmsd and Ado–A_1R distance in the three replicates of simulations are depicted in *SI Appendix*, Fig. S6 *A* and *B*. These simulations were performed on the model with truncation at residue $Ser6^{1.29}$. In addition, we performed another simulation on a model with the five N-terminal residues added (*SI Appendix*, Fig. S7), and this simulation showed a binding process similar to that discussed above.

"Open" and "closed" states of the orthosteric pocket. Most noteworthy, we observed that the orthosteric pocket was open and closed in the antagonist-bound A_1R (inactive state, PDB code 5N2S) and in the Ado–G_{i2}–bound A_1R (active state, PDB code 6D9H), similar to M_2R (37), in that the triangle perimeters of the $Glu170^{ECL2}$–$Tyr271^{7.36}$–$Glu172^{ECL2}$ "vestibular lid" (defined as the sum of the length of all three sides of the triangle composed of the side chain C_δ atoms of $Glu170^{ECL2}$ and $Glu172^{ECL2}$ and the side chain oxygen atom of $Tyr271^{7.36}$, shown in yellow dashed lines in Fig. 2*A*) were 31.1 Å (open) and 20.9 Å (closed), respectively. The triangle perimeter of the $Glu170^{ECL2}$–$Tyr271^{7.36}$–$Glu172^{ECL2}$ vestibular lid was monitored along the Ado–A_1R recognition process (Fig. 2*E*). When the Ado was removed from the orthosteric pocket and free in the solvent, the vestibular lid was closed. Following that, the vestibular lid gradually opened for Ado to enter the orthosteric binding site of A_1R. At the end of the Su-GaMD simulation, Ado reached a position similar to that in the active Ado–A_1R–G_{i2} 6D9H structure, and the vestibular lid was closed again. Thus, we observed the closed–open–closed conformational switch of the vestibular lid during the Ado–A_1R recognition process. In addition, the $Glu172^{ECL2}$–$Lys265^{ECL3}$ salt bridge was regarded as a hindrance of the orthosteric site (36, 44, 45). We also monitored the $Glu172^{ECL2}$–$Lys265^{ECL3}$ salt bridge (calculated based on the minimum distance between the side chain nitrogen atom of $Lys265^{ECL3}$ and the two carbonyl oxygens of $Glu172^{ECL2}$) in our simulations (*SI Appendix*, Fig. S8). The $Glu172^{ECL2}$–$Lys265^{ECL3}$ salt bridge showed a similar closed–open–closed conformational switch to the vestibular lid during the Ado–A_1R recognition process.

Recognition pathway of G_{i2} to A_1R. Immediately after the formation of the Ado–A_1R complex, we investigated the recognition pathway of G_{i2} to the active A_1R. Starting from free diffusion in the solvent, in which the $G\alpha_i$ rmsd was 83.7 Å and the A_1R–$G\alpha_i$ distance was 78.8 Å, G_{i2} gradually entered the intracellular binding site of A_1R in the 53.4-ns Su-GaMD simulation (Fig. 3*A*, Movie S2). During the Su-GaMD simulation of the A_1R–G_{i2} recognition process, the $G\alpha_i$ rmsd decreased to 2.7 Å (Fig. 3*C*) and the A_1R–$G\alpha_i$ distance decreased to 32.7 Å (see the black line in Fig. S6*D*), suggesting that the G_{i2} protein aligned well with that in the 6D9H structure at the end of the Su-GaMD simulation. The A_1R maintained in the activated state, in which the "ionic lock" was broken (with an N–O distance of >8 Å; Fig. 3*D*).

During the A_1R–G_{i2} recognition process, four metastable intermediate states (states a, b, c, and d) were identified (Fig. 3 *A* and *E*). In state a (at 21.600 ns), G_{i2} made initial contacts with the H8 region of A_1R ($Lys301^{8.56}$ in H8) through its α5-helix (state a in Fig. 3 *A* and *F*). In state b (at 33.450 ns), G_{i2} made further contacts with ICL1 in addition to H8 of A_1R (i.e., $Asn37^{1.60}$, $Ala39^{ICL1}$, $Gln293^{8.48}$, and $Lys294^{8.49}$, state b in Fig. 3 *A* and *F*), and the A_1R–G_{i2} binding free energy was −12.9 kcal/mol (state b in Fig. 3*E*). Then, G_{i2} entered the cavity composed of TM3, TM4, ICL2, TM5, and TM6 by contacting $Arg108^{3.53}$, $Thr112^{4.38}$, $Tyr115^{ICL2}$, $Lys116^{ICL2}$, $Gln210^{5.68}$, $Lys214^{5.72}$, and $Lys228^{6.29}$ of A_1R at 43.500 ns (state c in Fig. 3 *A* and *F*). The A_1R–G_{i2} binding free energy decreased to −33.8 kcal/mol in state c (state c in Fig. 3*E*). Finally (state d, at 53.100 ns), G_{i2} moved into the much deeper intracellular binding pocket of A_1R and interacted with A_1R through residues $Gln38^{ICL1}$, $Arg105^{3.50}$, $Arg108^{3.53}$, $Val109^{3.54}$, $Thr112^{4.38}$, $Leu113^{ICL2}$, $Arg114^{ICL2}$, $Tyr115^{ICL2}$, $Lys116^{ICL2}$, $Tyr205^{5.63}$, $Arg208^{5.66}$, $Gln210^{5.68}$, $Lys213^{5.71}$, $Lys214^{5.72}$, $Lys228^{6.29}$, $Glu229^{6.30}$, $Lys231^{6.32}$, $Leu236^{6.37}$, and $Lys294^{H8}$ (state d in Fig. 3 *A* and *F*). The binding free energy decreased to −36.5 kcal/mol in state d (state d in Fig. 3*E*). G_{i2} eventually entered the intracellular pocket and formed stable interactions with A_1R at the end of the Su-GaMD simulation. The interaction interface was composed of TM3, ICL2, TM5-TM7, and H8 of A_1R and the α5-helix, α*N*-helix, and α*N*-β1 loop of G_{i2}. All the key molecular interactions between A_1R and G_{i2} in the 6D9H structure and state d are included in *SI Appendix*, Table S5. Five of the seven interactions in the 6D9H structure were observed to maintained in state d. Specifically, $Gln210^{5.68}$ and $Lys228^{6.29}$ of A_1R formed hydrogen bonds with Asp342 and Phe355 of the α5-helix of G_{i2}, and $Arg108^{3.53}$, $Lys294^{H8}$, and $Lys213^{5.71}$ of A_1R formed salt bridges with Asp351 and Asp342 of the α5-helix of G_{i2} (*SI Appendix*, Table S5 and Fig. 3*B*). Thus, the structure of state d predicted by the Su-GaMD simulation revealed a similar mode of interaction compared with the A_1R–G_{i2} complex in the 6D9H structure. We can see from the contact residues in states a to d that the ICLs (especially ICL2) of A_1R formed favorable contacts with G_{i2}, and they played an important role in the recognition and binding of the G_{i2} protein. This important role of ICLs in A_1R–G_{i2} recognition is consistent with the previous long-timescale simulation of nanobody Nb9-8 to M_2R (37).

To intuitively exhibit the evolution of interactions between A_1R and G_{i2} during the binding process, we performed protein residue network analyses. The networks between A_1R and G_{i2} for states a to d are shown in *SI Appendix*, Fig. S9. It was seen that the network strength between A_1R and G_{i2} increased gradually during the recognition process.

Three independent MD simulations showed similar results. The $G\alpha_i$ rmsd and A_1R–$G\alpha_i$ distance during the A_1R–G_{i2} recognition of the three replicates are depicted in *SI Appendix*, Fig. S6 *C* and *D*. Similar to previous studies (8, 46), the helical domain of G_{i2} that was not included in the cryo-EM structures was omitted in these simulations. This was based on the fact that the helical domain did not form direct contact with the atoms of A_1R in the A_1R–G_{i2} ternary complex. In addition, we performed another simulation on a model with the helical domain rebuilt, and this simulation showed a similar A_1R–G_{i2} recognition process to that discussed above (*SI Appendix*, Fig. S10).

In summary, we reconstructed the Ado–A_1R–G_{i2} complex from A_1R (in its active state) and free Ado and G_{i2} using the Su-GaMD approach. The reconstruction process involved two stages, as follows: the Ado–A_1R binding event (25.8 ns of supervision on Ado rmsd) and the A_1R–G_{i2} binding event (53.4 ns of supervision on $G\alpha_i$ rmsd). The $Glu170^{ECL2}$–$Tyr271^{7.36}$–$Glu172^{ECL2}$ vestibular lid and the $Glu172^{ECL2}$–$Lys265^{ECL3}$ salt bridge showed a closed–open–closed conformational switch

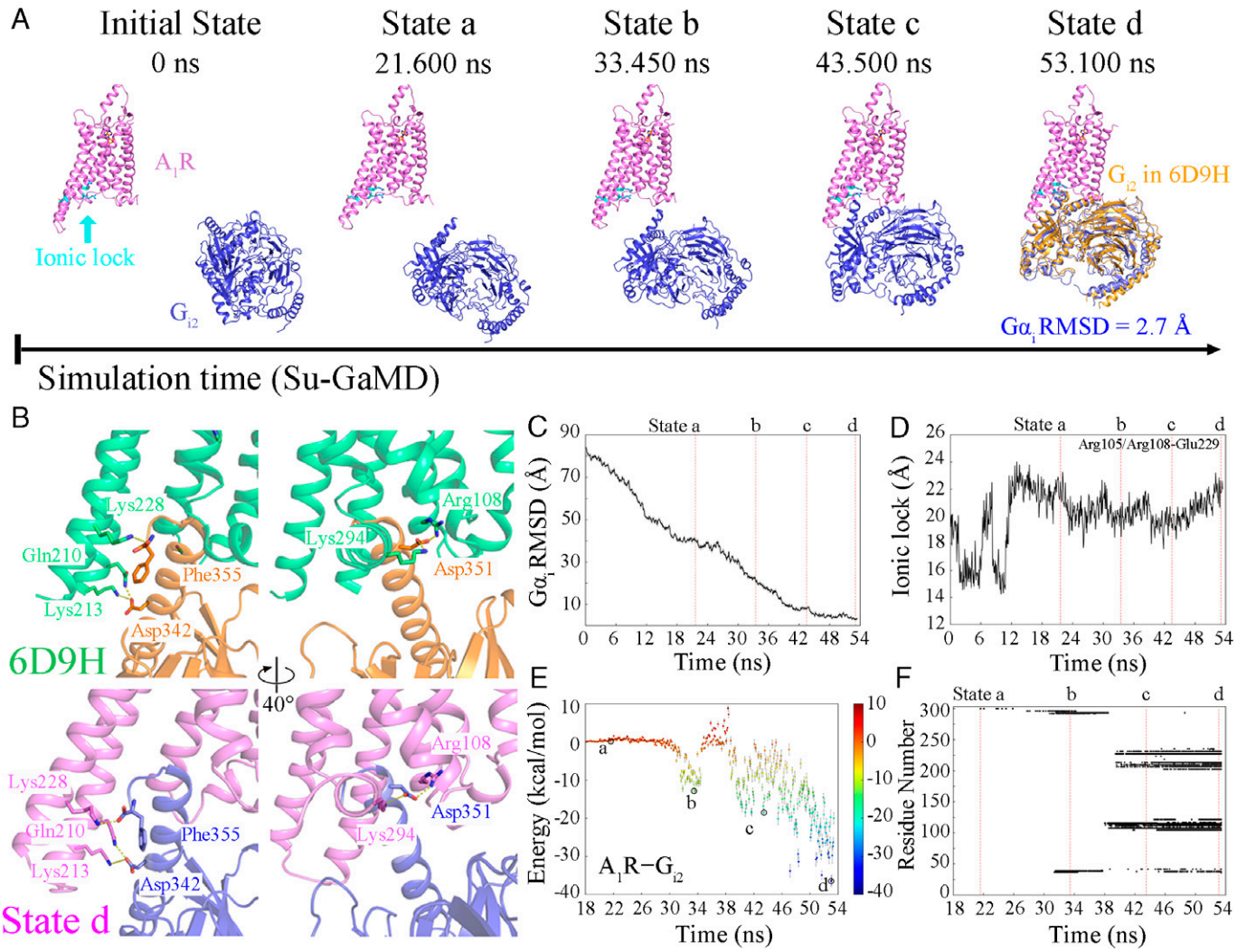

Fig. 3. (*A*) The landscape of the A_1R–G_{i2} recognition pathway. The relative position of G_{i2} after global alignment of A_1R (A_1R is shown in violet, and G_{i2} is shown in blue) to that of the 6D9H structure (G_{i2} is shown in orange) is shown in state d. (*B*) The same key molecular interactions in the 6D9H structure (A_1R and G_{i2} are shown in green and orange, respectively) and state d (A_1R and G_{i2} are shown in violet and blue, respectively). Time-dependent (*C*) $G\alpha_i$ rmsd, (*D*) N–O distance between the guanidinium of $Arg105^{3.50}$/$Arg108^{3.53}$ and the carboxyl of $Glu229^{6.30}$, (*E*) the binding free energy landscape for A_1R–G_{i2}, and (*F*) A_1R–G_{i2} contact residues during the recognition process.

during the Ado–A_1R binding event, and the ICLs played important roles in the A_1R–G_{i2} binding event.

Full Activation Mechanism of A_1R: Reconstruction of the Ado–A_1R–G_{i2} Complex from the Inactive A_1R Structure. The full activation process of A_1R from its inactive state was captured after its recognition with both Ado and G_{i2}. The whole reconstruction process of the Ado–A_1R–G_{i2} complex from the inactive A_1R (i.e., the full activation mechanism of A_1R) included three events, as follows: the Ado–A_1R binding event, the A_1R preactivation event just before G_{i2} binds to A_1R, and the A_1R–G_{i2} binding event. Consequently, three stages of simulations were performed to investigate the whole activation process (Fig. 4 *A* and *B*). The first stage was an 82.2-ns Su-GaMD simulation to investigate the Ado–A_1R binding event (Su-GaMD-1, with the Ado rmsd supervised). The second stage was a 150-ns GaMD simulation to investigate the A_1R conformational changes from the inactive state to the preactive state. The third stage was a 55.2-ns Su-GaMD simulation to investigate the A_1R–G_{i2} binding event from the preactive Ado–A_1R complex (Su-GaMD-2, with $G\alpha_i$ rmsd supervised). A ternary Ado–A_1R–G_{i2} complex was achieved at the end of these three stages of simulations (*SI Appendix*, Fig. S11). The animations of the Ado–A_1R binding event, the A_1R preactivation event, and the A_1R–G_{i2} binding event are shown in Movies S3–S5.

In the events involved in the A_1R full activation process, we monitored the conformational changes of the vestibular lid of the orthosteric pocket and the ionic lock between $Arg105^{3.50}$/$Arg108^{3.53}$ and $Glu229^{6.30}$ (Fig. 4 *C* and *D*). Four states of A_1R were captured during the simulations, in which the characters involved in the full A_1R activation process were clearly stated in the time sequence (states a*, b*, c* and final state in Fig. 4*E*).

Ado–A_1R recognition. Ado entered the orthosteric site of A_1R, which made A_1R reach state a* at 61.200 ns in Su-GaMD-1 (state a* in Fig. 4*E*). In state a*, the hydrogen in the 6-amino group of the purine ring of Ado formed a hydrogen bond with the oxygen atom of the amide group of $Asn254^{6.55}$, which helped Ado locate the orthosteric site of A_1R (state a* in Fig. 4*E*). The extracellular vestibular lid was fully open in state a* (with the $Glu170^{ECL2}$–$Tyr271^{7.36}$–$Glu172^{ECL2}$ triangle perimeter of 40.2 Å, state a* in Fig. 4*C*). Afterward, at 82.200 ns in Su-GaMD-1, Ado adjusted its orientation in the orthosteric pocket and possessed a binding mode consistent with the 6D9H structure (state b* in Fig. 4*E*). After Ado entered the orthosteric

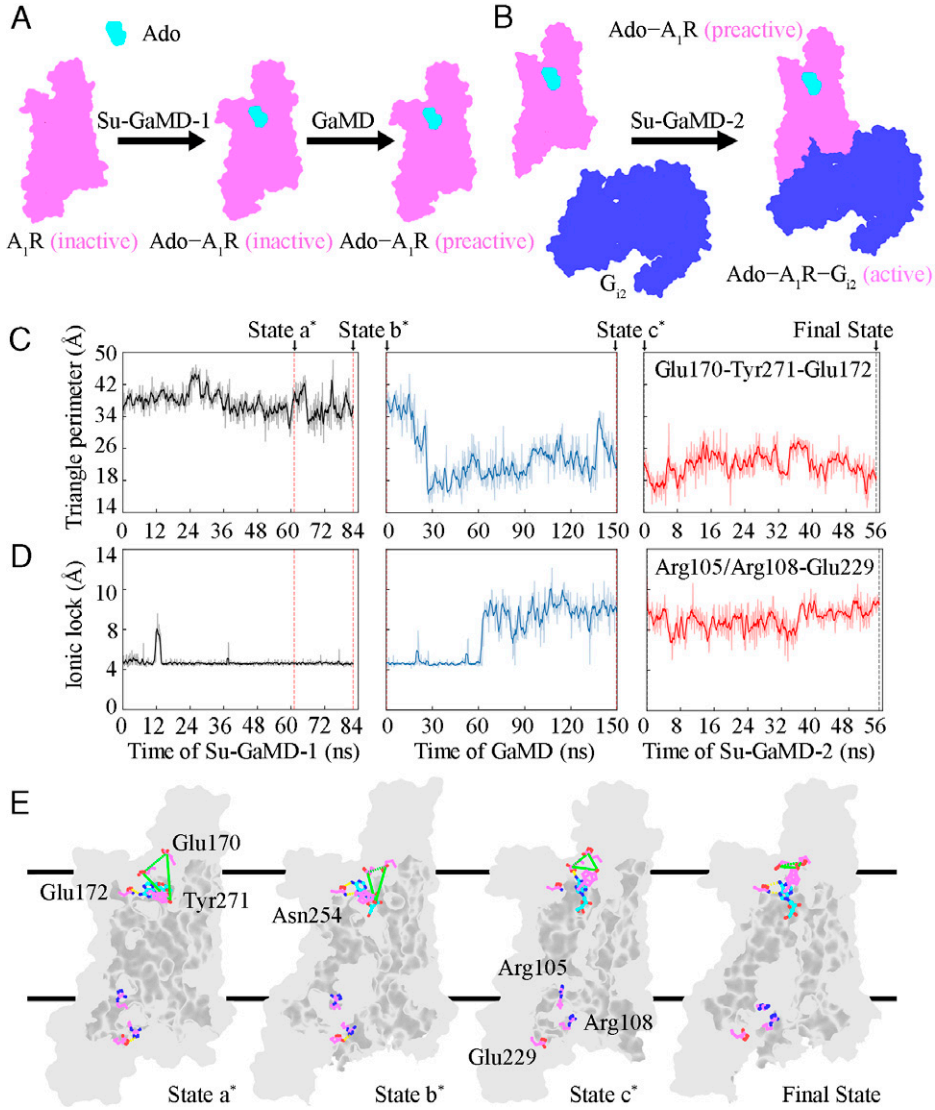

Fig. 4. Schematic diagram of the reconstruction process of the Ado−A_1R−G_{i2} complex from inactive A_1R, including (*A*) the Ado−A_1R binding event and the A_1R preactivation event and (*B*) the A_1R−G_{i2} binding event. Ado (cyan outline), A_1R (violet outline), and G_{i2} (blue outline) are shown in surface model. Time dependent (*C*) triangle perimeter of the Glu170^{ECL2}–Tyr271$^{7.36}$–Glu172^{ECL2} vestibular lid and (*D*) N–O distance between the guanidinium of Arg105$^{3.50}$/Arg108$^{3.53}$ and the carboxyl of Glu229$^{6.30}$ during the whole activation process. (*E*) Representative structures of A_1R during the whole activation process. A_1R is displayed as a gray surface model. Ado (cyan) and key residues in A_1R (violet) are displayed in ball-and-stick. The Glu170^{ECL2}–Tyr271$^{7.36}$–Glu172^{ECL2} vestibular lid is depicted by green dashed lines, and hydrogen bonds are depicted by yellow dashed lines.

pocket of A_1R, the vestibular lid was still open (with a Glu170^{ECL2}–Tyr271$^{7.36}$–Glu172^{ECL2} triangle perimeter of 33.2 Å, state b* in Fig. 4*C*). The ionic lock between Arg105$^{3.50}$/Arg108$^{3.53}$ and Glu229$^{6.30}$ was still closed (with an N–O distance of 4.0 Å, state b* in Fig. 4*D*) in state b*, which means that A_1R remained in the inactive state.

Preactivation of A_1R. We performed three parallel 150-ns GaMD simulations and simulated the A_1R from the inactive state to the preactive state. At the end of the 150-ns GaMD simulation, the Ado rmsd and the A_1R rmsd (defined as the rmsd calculated on the heavy atoms of A_1R (without including TM6) relative to the 6D9H structure) were 1.5 Å and 2.0 Å, the ionic lock between Arg105$^{3.50}$/Arg108$^{3.53}$ and Glu229$^{6.30}$ was broken (with N–O distance of >8 Å, state c* in Fig. 4*D*), and the A_1R achieved the preactive state (state c* in Fig. 4*E*), in which its ionic lock was broken but had not reached the full activation state of the G_{i2}-bound state. The vestibular lid changed to be closed (with the Glu170^{ECL2}–Tyr271$^{7.36}$–Glu172^{ECL2} triangle perimeter of 22.9 Å, state c* in Fig. 4*C*) in the preactive state. For comparison, we also performed three parallel 300-ns GaMD simulations for apo-A_1R. The results in *SI Appendix*, Fig. S12 show that the ionic lock between Arg105$^{3.50}$/Arg108$^{3.53}$ and Glu229$^{6.30}$ did not break during the three parallel simulations for the apo-A_1R system. In contrast, the A_1R achieved the preactive state (characterized by the breaking of the ionic lock) after the 150-ns GaMD simulations of the Ado-A_1R system. These results indicated that the preactivation of A_1R was the consequence of the Ado binding event. This preactivation of A_1R is in agreement with the preactivated complex in the combined activation mechanism of a class B GPCR glucagon receptor revealed by Mattedi et al. (47) with MTD simulations.

Recognition between preactivated A_1R and G_{i2}. The landscape of the A_1R–G_{i2} recognition pathway from the preactive state of A_1R is shown in *SI Appendix*, Fig. S11*A*. At 55.200 ns in Su-GaMD-2, the Ado–A_1R–G_{i2} complex was achieved (final state in Fig. 4*E* and *SI Appendix*, Fig. S11*A*), and this structure aligned well with the 6D9H structure (with an Ado rmsd of 2.0 Å, an A_1R rmsd of 1.7 Å, and a Gα_i rmsd of 2.9 Å; *SI Appendix*,

Fig. S11 *B–F*). In the final state, the ionic lock broke (final state in Fig. 4*E*), the intracellular half of TM6 moved outward, and the bend angle (between the Cα atoms of Tyr225$^{6.26}$, Leu245$^{6.46}$, and Thr257$^{6.58}$) of TM6 increased to 151.1°, which was comparable to the bend angle of 153.5° in the 6D9H structure. These results indicated that A_1R was fully activated in the final state. When A_1R was fully activated, the vestibular lid was closed (with the Glu170^{ECL2}–Tyr271$^{7.36}$–Glu172^{ECL2} triangle perimeter of 22.0 Å that was comparable to that of 20.9 Å in the 6D9H structure, see final state in Fig. 4*C*). Three independent MD simulations for each stage showed similar results. The Ado rmsds and Ado–A_1R distances of the three replicates of Su-GaMD-1 trajectories as well as the $G\alpha_i$ rmsds and A_1R–$G\alpha_i$ distances of the three replicates of Su-GaMD-2 trajectories are depicted in *SI Appendix*, Figs. S11 *C* and *E*, respectively. The A_1R rmsd of the three replicates of the three stages of simulations are depicted in *SI Appendix*, Fig. S11*F*.

For more comparisons between Su-MD and Su-GaMD, we performed Su-MD simulations for the A_1R–G_{i2} recognition process from the preactive A_1R and G_{i2} (Su-MD-2, with $G\alpha_i$ rmsd supervised). The $G\alpha_i$ rmsds and $G\alpha_i$–A_1R distances in the three replicates of Su-MD-2 are depicted in *SI Appendix*, Fig. S13. The minimum $G\alpha_i$ rmsds and the minimum A_1R–$G\alpha_i$ distances of Su-GaMD-2 and Su-MD-2 are depicted in *SI Appendix*, Table S4. It was seen that the $G\alpha_i$ rmsds of Su-GaMD-2 could reach the target value (<5 Å) in less than 75.0 ns, while the $G\alpha_i$ rmsds of Su-MD-2 could not reach the target value (<5 Å) in more than 100.2 ns. These findings indicated that Su-MD needs more computational cost than Su-GaMD in the simulation of the protein–protein recognition process.

G_{i2}-induced conformational changes feed back to the orthosteric pocket in A_1R. More interestingly, we observed coupling between the Ado–A_1R and A_1R–G_{i2} binding events by calculating the Ado–A_1R binding free energies and the volumes of the Ado-binding pocket in A_1R for the four states during the whole activation process (Table 2). The volume change of the Ado-binding pocket and the G_{i2}-binding site during the full activation process is shown in *SI Appendix*, Fig. S14. On the intracellular side, the volumes of the G_{i2}-binding site in the inactive 5N2S and the active 6D9H structures were 797.9 Å^3 and 1632.1 Å^3, respectively. During the whole activation process, the volume of the G_{i2}-binding site dilated from 908.3 Å^3 in state a* (comparable to that in the inactive 5N2S structure) to 1,768.0 Å^3 in the final state (comparable to that in the active 6D9H structure). On the extracellular side, the volumes of the Ado–binding pocket in the inactive 5N2S and the active 6D9H structures were 424.0 Å^3 and 318.9 Å^3, respectively, which indicated shrinkage of the pocket after the full activation of A_1R. During the reconstruction process of the Ado–A_1R–G_{i2} complex, the volume of the Ado–binding pocket in A_1R shrank from 463.9 Å^3 in state a* (comparable to that in the inactive 5N2S structure) to 321.4 Å^3 in the final state (comparable to that in the active 6D9H structure). As a result of the volume decrease of the Ado-binding pocket in A_1R, the Ado–A_1R binding free energy decreased from −12.1 kcal/mol in state a* to −34.0 kcal/mol in the final state (comparable to the binding free energy of −34.2 kcal/mol in the fully active 6D9H structure). These results suggested that the intracellular binding of G_{i2} to A_1R showed a benefit in shrinking the extracellular orthosteric binding site and promoting the binding affinity of Ado in A_1R. These results reflected the allosteric coupling between the intracellular G_{i2} protein binding and the conformational changes in the extracellular orthosteric Ado-binding pocket of A_1R. This observation was consistent with previous experimental studies for another class A GPCR, β_1AR, in which the active-state structures of β_1AR with the nanobody that exhibited G protein-like behavior binding in the intracellular site showed a 24 to 42% reduction in the volume of the extracellular orthosteric ligand-binding pocket compared with the inactive-state structures (48).

Table 2. The volumes of the Ado−binding pocket and the Ado−A_1R binding free energies for the 5N2S and 6D9H structures and states a*, b*, c* and the final state

Entry	Ado−binding pocket volume (SE, Å^3)	Ado−A_1R binding free energy (SE, kcal/mol)
5N2S structure	424.0	–
6D9H structure	318.9	−34.2 (1.2)*
State a*	463.9 (15.3)†	−12.1 (1.1)†
State b*	433.0 (12.2)†	−11.8 (1.1)†
State c*	331.5 (11.7)†	−24.5 (1.4)†
Final state	321.4 (10.5)†	−34.0 (1.1)†

*We performed 100 ns cMD simulations for the 6D9H structure embedded in POPC in a water box and extracted the last 1.2-ns trajectory to calculate the Ado−A_1R binding free energy.

†We extracted the 1.2-ns trajectory prior to the frame of states a*, b*, c* and the final state to calculate the volume of the Ado-binding pocket and the Ado−A_1R binding free energy, respectively.

Conclusions

In the present work, we developed a Su-GaMD approach by incorporating a tabu-like supervision algorithm into a standard GaMD simulation. The Su-GaMD simulations allowed us to identify the binding pathways and important intermediate states of the ligand and the G protein recognitions to GPCR. We successfully used this Su-GaMD method to investigate Ado–A_1R recognition and the subsequent A_1R–G_{i2} recognition event within hundreds of nanoseconds of simulations. The possible recognition pathways and important intermediate states of the Ado–A_1R and A_1R–G_{i2} binding events were identified, the Ado–A_1R–G_{i2} complex was reconstructed from both active and inactive A_1R, and the full activation mechanism of A_1R (i.e., the whole signaling process from the extracellular side to the intracellular side of A_1R) was revealed. Starting from free diffusion in the solvent, Ado gradually entered the extracellular orthosteric site of A_1R. After that, A_1R achieved the preactive state that was characterized by the broken ionic lock between Arg105$^{3.50}$/Arg108$^{3.53}$ and Glu229$^{6.30}$ on the intracellular side. Then, G_{i2} recognized the intracellular binding site and bound to A_1R, the Ado–A_1R–G_{i2} complex was reconstructed, and A_1R was fully activated. The binding of Ado to the extracellular orthosteric site A_1R initiates conformational changes and the preactivation of A_1R. In turn, the binding of G_{i2} to the intracellular side of A_1R caused a decrease in the volume of the extracellular orthosteric pocket and stabilized the binding of Ado. These results reflect the allosteric coupling between the intracellular G_{i2} protein binding and the conformational change in the extracellular orthosteric Ado-binding pocket of A_1R. With this case study of A_1R, we have proven the applicability of the Su-GaMD approach to reconstruct a ligand–GPCR–G protein complex in nanosecond-timescale simulations, and the ligand–GPCR and GPCR–G protein recognition pathways were identified.

Molecular biologists have recently focused on the key conformational states and molecular details provided by a significant number of experimentally resolved ligand–GPCR or GPCR–G protein structures. On the one hand, it is more urgent to understand how the binding complexes are formed and to

define the transformation process between the key conformational states over time. Distinguished conformational states in the G protein signaling pathway have been previously resolved by excellent experimental scientists, and it is necessary to connect these states by computational approaches. On the other hand, the future of drug design will involve detailed characterization of experimentally resolved bound states as well as the metastable intermediate states (metabinding sites) predicted by computational techniques with more efficiency. Su-GaMD simulations for A_1R provide a promising approach that can both predict the binding complexes and reveal the metastable intermediate states in the full activation process of A_1R. Taken together, the computationally determined full activation mechanism provides comprehensive insights into the A_1R activation process and contributes to the future design of small molecules that could bias the signaling of A_1R.

Materials and Methods

All MD simulations were carried out using Amber 18 (49). The AMBER FF14SB force field (50) was used for proteins, the general AMBER force field (GAFF) (51) was used for ligands, and the AMBER lipid force field LIPID14 (52) was used for 1-palmitoyl-2-oleoyl-sn-glycero-3-phosphorylcholines (POPCs). Ado and G_{i2} were separately placed >20 Å away from A_1R to reconstruct a ternary complex of Ado, G_{i2}, and A_1R (Ado–A_1R–G_{i2}) from both active and inactive A_1R. The Ado–A_1R recognition event and the A_1R–G_{i2} recognition event were investigated by using the Su-GaMD method with the rmsds of Ado or G_{i2} protein supervised. For the inactive system, a 150-ns GaMD simulation was performed to obtain a preactive state of A_1R before the A_1R–G_{i2} recognition event was simulated. Further details are provided in *SI Appendix*.

Data, Materials, and Software Availability. All study data are included in the article and/or supporting information. The data have not been deposited in a publicly accessible database.

ACKNOWLEDGMENTS. This work was supported by the China Postdoctoral Science Foundation (Grant No. BSMS69004).

Author affiliations: [a]State Key Laboratory of Medicinal Chemical Biology, Frontiers Science Center for Cell Responses, College of Pharmacy and Tianjin Key Laboratory of Molecular Drug Research, Nankai University, Tianjin 300350, China; [b]College of Life Sciences, Nankai University, Tianjin 300350, China; [c]Biodesign Center, Tianjin Institute of Industrial Biotechnology, Chinese Academy of Sciences, Tianjin 300308, China; and [d]Platform of Pharmaceutical Intelligence, Tianjin International Joint Academy of Biomedicine, Tianjin 300457, China

Author contributions: Y.L., D.L., and J.L. designed research; Y.L. and J.S. performed research; Y.L., D.L., and J.L. analyzed data; and Y.L., D.L., and J.L. wrote the paper.

1. K. Sriram, P. A. Insel, G protein-coupled receptors as targets for approved drugs: How many targets and how many drugs? *Mol. Pharmacol.* **93**, 251–258 (2018).
2. N. R. Latorraca, A. J. Venkatakrishnan, R. O. Dror, GPCR dynamics: Structures in motion. *Chem. Rev.* **117**, 139–155 (2017).
3. T. Kenakin, Theoretical aspects of GPCR-ligand complex pharmacology. *Chem. Rev.* **117**, 4–20 (2017).
4. M. Congreve, C. de Graaf, N. A. Swain, C. G. Tate, Impact of GPCR structures on drug discovery. *Cell* **181**, 81–91 (2020).
5. H. Gutiérrez-de-Terán, J. Sallander, E. Sotelo, Structure-based rational design of adenosine receptor ligands. *Curr. Top. Med. Chem.* **17**, 40–58 (2017).
6. B. B. Fredholm, A. P. IJzerman, K. A. Jacobson, J. Linden, C. E. Müller, Nomenclature and classification of adenosine receptors–An update. *Pharmacol. Rev.* **63**, 1–34 (2011).
7. M. J. Zylka, Pain-relieving prospects for adenosine receptors and ectonucleotidases. *Trends Mol. Med.* **17**, 188–196 (2011).
8. C. J. Draper-Joyce *et al.*, Positive allosteric mechanisms of adenosine A_1 receptor-mediated analgesia. *Nature* **597**, 571–576 (2021).
9. M. J. Wall *et al.*, Selective activation of Gαob by an adenosine A_1 receptor agonist elicits analgesia without cardiorespiratory depression. *Nat. Commun.* **13**, 4150 (2022).
10. D. Guo, L. H. Heitman, A. P. IJzerman, Kinetic aspects of the interaction between ligand and G protein-coupled receptor: The case of the adenosine receptors. *Chem. Rev.* **117**, 38–66 (2017).
11. R. Romagnoli, P. G. Baraldi, A. R. Moorman, P. A. Borea, K. Varani, Current status of A_1 adenosine receptor allosteric enhancers. *Future Med. Chem.* **7**, 1247–1259 (2015).
12. S. Kashfi, K. Ghaedi, H. Baharvand, M. H. Nasr-Esfahani, M. Javan, A_1 adenosine receptor activation modulates central nervous system development and repair. *Mol. Neurobiol.* **54**, 8128–8139 (2017).
13. J. F. Chen, H. K. Eltzschig, B. B. Fredholm, Adenosine receptors as drug targets–What are the challenges? *Nat. Rev. Drug Discov.* **12**, 265–286 (2013).
14. K. A. Jacobson, Z. G. Gao, Adenosine receptors as therapeutic targets. *Nat. Rev. Drug Discov.* **5**, 247–264 (2006).
15. A. Glukhova *et al.*, Structure of the Adenosine A1 Receptor Reveals the Basis for Subtype Selectivity. *Cell* **168**, 867–877.e13 (2017).
16. R. K. Y. Cheng *et al.*, Structures of Human A1 and A2A Adenosine Receptors with Xanthines Reveal Determinants of Selectivity. *Structure* **25**, 1275–1285.e4 (2017).
17. C. J. Draper-Joyce *et al.*, Structure of the adenosine-bound human adenosine A_1 receptor-G_i complex. *Nature* **558**, 559–563 (2018).
18. P. Fronik, B. I. Gaiser, D. Sejer Pedersen, Bitopic ligands and metastable binding sites: Opportunities for G protein-coupled receptor (GPCR) medicinal chemistry. *J. Med. Chem.* **60**, 4126–4134 (2017).
19. Y. Du *et al.*, Assembly of a GPCR-G protein complex. *Cell* **177**, 1232–1242.e11 (2019).
20. D. M. Rosenbaum *et al.*, Structure and function of an irreversible agonist-$\beta(_2)$ adrenoceptor complex. *Nature* **469**, 236–240 (2011).
21. R. O. Dror *et al.*, Pathway and mechanism of drug binding to G-protein-coupled receptors. *Proc. Natl. Acad. Sci. U.S.A.* **108**, 13118–13123 (2011).
22. Q. Bai, D. Shi, Y. Zhang, H. Liu, X. Yao, Exploration of the antagonist CP-376395 escape pathway for the corticotropin-releasing factor receptor 1 by random acceleration molecular dynamics simulations. *Mol. Biosyst.* **10**, 1958–1967 (2014).
23. V. Ísberg, T. Balle, T. Sander, F. S. Jørgensen, D. E. Gloriam, G protein- and agonist-bound serotonin 5-HT_{2A} receptor model activated by steered molecular dynamics simulations. *J. Chem. Inf. Model.* **51**, 315–325 (2011).
24. N. Saleh, P. Ibrahim, T. Clark, Differences between G-protein-stabilized agonist-GPCR complexes and their nanobody-stabilized equivalents. *Angew. Chem. Int. Ed. Engl.* **56**, 9008–9012 (2017).
25. Y. Miao, S. E. Nichols, P. M. Gasper, V. T. Metzger, J. A. McCammon, Activation and dynamic network of the M_2 muscarinic receptor. *Proc. Natl. Acad. Sci. U.S.A.* **110**, 10982–10987 (2013).
26. D. Hamelberg, J. Mongan, J. A. McCammon, Accelerated molecular dynamics: A promising and efficient simulation method for biomolecules. *J. Chem. Phys.* **120**, 11919–11929 (2004).
27. A. C. Kruse *et al.*, Structure and dynamics of the M_3 muscarinic acetylcholine receptor. *Nature* **482**, 552–556 (2012).
28. D. Provasi, A. Bortolato, M. Filizola, Exploring molecular mechanisms of ligand recognition by opioid receptors with metadynamics. *Biochemistry* **48**, 10020–10029 (2009).
29. L. M. Wingler, C. McMahon, D. P. Staus, R. J. Lefkowitz, A. C. Kruse, Distinctive Activation Mechanism for Angiotensin Receptor Revealed by a Synthetic Nanobody. *Cell* **176**, 479–490.e12 (2019).
30. I. Shimada, T. Ueda, Y. Kofuku, M. T. Eddy, K. Wüthrich, GPCR drug discovery: Integrating solution NMR data with crystal and cryo-EM structures. *Nat. Rev. Drug Discov.* **18**, 59–82 (2019).
31. D. Sabbadin, S. Moro, Supervised molecular dynamics (SuMD) as a helpful tool to depict GPCR-ligand recognition pathway in a nanosecond time scale. *J. Chem. Inf. Model.* **54**, 372–376 (2014).
32. S. Bhattacharya, N. Vaidehi, Mechanism of allosteric communication in GPCR activation from microsecond scale molecular dynamics simulations. *Biophys. J.* **112**, 498a–499a (2017).
33. S. Yuan *et al.*, The molecular mechanism of $P2Y_1$ receptor activation. *Angew. Chem. Int. Ed. Engl.* **55**, 10331–10335 (2016).
34. Y. Li, J. Sun, D. Li, J. Lin, Activation and conformational dynamics of a class B G-protein-coupled glucagon receptor. *Phys. Chem. Chem. Phys.* **18**, 12642–12650 (2016).
35. Y. Zhou *et al.*, Molecular insights into ligand recognition and G protein coupling of the neuromodulatory orphan receptor GPR139. *Cell Res.* **32**, 210–213 (2022).
36. G. Deganutti *et al.*, Deciphering the agonist binding mechanism to the adenosine A_1 receptor. *ACS Pharmacol. Transl. Sci.* **4**, 314–326 (2021).
37. Y. Miao, J. A. McCammon, Mechanism of the G-protein mimetic nanobody binding to a muscarinic G-protein-coupled receptor. *Proc. Natl. Acad. Sci. U.S.A.* **115**, 3036–3041 (2018).
38. V. Salmaso, M. Sturlese, A. Cuzzolin, S. Moro, Exploring Protein-Peptide Recognition Pathways Using a Supervised Molecular Dynamics Approach. *Structure* **25**, 655–662.e2 (2017).
39. A. Cuzzolin *et al.*, Deciphering the complexity of ligand-protein recognition pathways using supervised molecular dynamics (SuMD) simulations. *J. Chem. Inf. Model.* **56**, 687–705 (2016).
40. D. Sabbadin *et al.*, Exploring the recognition pathway at the human A_{2A} adenosine receptor of the endogenous agonist adenosine using supervised molecular dynamics simulations. *MedChemComm* **6**, 1081–1085 (2015).
41. G. Deganutti, A. Welihinda, S. Moro, Comparison of the human A_{2A} adenosine receptor recognition by adenosine and inosine: New insight from supervised molecular dynamics simulations. *ChemMedChem* **12**, 1319–1326 (2017).
42. A. T. N. Nguyen *et al.*, Extracellular loop 2 of the adenosine A_1 receptor has a key role in orthosteric ligand affinity and agonist efficacy. *Mol. Pharmacol.* **90**, 703–714 (2016).
43. Y. Miao, A. Bhattarai, A. T. N. Nguyen, A. Christopoulos, L. T. May, Structural basis for binding of allosteric drug leads in the adenosine A_1 receptor. *Sci. Rep.* **8**, 16836 (2018).
44. W. Jespers *et al.*, Structural mapping of adenosine receptor mutations: Ligand binding and signaling mechanisms. *Trends Pharmacol. Sci.* **39**, 75–89 (2018).
45. G. Mattedi, F. Deflorian, J. S. Mason, C. de Graaf, F. L. Gervasio, Understanding ligand binding selectivity in a prototypical GPCR family. *J. Chem. Inf. Model.* **59**, 2830–2836 (2019).
46. J. Wang, Y. Miao, Mechanistic insights into specific G protein interactions with adenosine receptors. *J. Phys. Chem. B* **123**, 6462–6473 (2019).
47. G. Mattedi, S. Acosta-Gutiérrez, T. Clark, F. L. Gervasio, A combined activation mechanism for the glucagon receptor. *Proc. Natl. Acad. Sci. U.S.A.* **117**, 15414–15422 (2020).
48. T. Warne, P. C. Edwards, A. S. Doré, A. G. W. Leslie, C. G. Tate, Molecular basis for high-affinity agonist binding in GPCRs. *Science* **364**, 775–778 (2019).
49. D. A. Case *et al.*, *AMBER 2018* (University of California, San Francisco, 2018).
50. J. A. Maier *et al.*, ff14SB: Improving the accuracy of protein side chain and backbone parameters from ff99SB. *J. Chem. Theory Comput.* **11**, 3696–3713 (2015).
51. J. Wang, R. M. Wolf, J. W. Caldwell, P. A. Kollman, D. A. Case, Development and testing of a general amber force field. *J. Comput. Chem.* **25**, 1157–1174 (2004).
52. C. J. Dickson *et al.*, Lipid14: The Amber lipid force field. *J. Chem. Theory Comput.* **10**, 865–879 (2014).